

Reliable computational design of biological-inorganic materials to the large nanometer scale using Interface-FF

Chamila C. Dharmawardhana, Krishan Kanhaiya, Tzu-Jen Lin, Amanda Garley, Marc R. Knecht, Jihan Zhou, Jianwei Miao & Hendrik Heinz

To cite this article: Chamila C. Dharmawardhana, Krishan Kanhaiya, Tzu-Jen Lin, Amanda Garley, Marc R. Knecht, Jihan Zhou, Jianwei Miao & Hendrik Heinz (2017) Reliable computational design of biological-inorganic materials to the large nanometer scale using Interface-FF, Molecular Simulation, 43:13-16, 1394-1405, DOI: [10.1080/08927022.2017.1332414](https://doi.org/10.1080/08927022.2017.1332414)

To link to this article: <http://dx.doi.org/10.1080/08927022.2017.1332414>



Published online: 19 Jun 2017.



Submit your article to this journal [↗](#)



Article views: 86



View related articles [↗](#)



View Crossmark data [↗](#)



Reliable computational design of biological-inorganic materials to the large nanometer scale using Interface-FF

Chamila C. Dharmawardhana^a, Krishan Kanhaiya^a, Tzu-Jen Lin^b, Amanda Garley^a, Marc R. Knecht^c, Jihan Zhou^d, Jianwei Miao^d and Hendrik Heinz^a

^aDepartment of Chemical and Biological Engineering, University of Colorado at Boulder, Boulder, CO, USA; ^bDepartment of Chemical Engineering, Chung Yuan Christian University, Taoyuan City, Taiwan, ROC; ^cDepartment of Chemistry, University of Miami, Coral Gables, FL, USA; ^dDepartment of Physics and Astronomy and California NanoSystems Institute, University of California, Los Angeles, CA, USA

ABSTRACT

The function of nanomaterials and biomaterials greatly depends on understanding nanoscale recognition mechanisms, crystal growth and surface reactions. The Interface Force Field (IFF) and surface model database are the first collection of transferable parameters for inorganic and organic compounds that can be universally applied to all materials. IFF uses common energy expressions and achieves best accuracy among classical force fields due to rigorous validation of structural and energetic properties of all compounds in comparison to perpetually valid experimental data. This paper summarises key aspects of parameterisation, including atomic charges and transferability of parameters and current coverage. Examples of biomolecular recognition at metal and mineral interfaces, surface reactions of alloys, as well as new models for graphitic materials and pi-conjugated molecules are described. For several metal–organic interfaces, a match in accuracy of computed binding energies between of IFF and DFT results is demonstrated at ten million times lower computational cost. Predictive simulations of biomolecular recognition of peptides on phosphate and silicate surfaces are described as a function of pH. The use of IFF for reactive molecular dynamics is illustrated for the oxidation of Mo₃Si alloys at high temperature, showing the development of specific porous silica protective layers. The introduction of virtual pi electrons in graphite and pi-conjugated molecules enables improvements in property predictions by orders of magnitude. The inclusion of such molecule-internal polarity in IFF can reproduce cation–pi interactions, pi-stacking in graphite, DNA bases, organic semiconductors and the dynamics of aqueous and biological interfaces for the first time.

ARTICLE HISTORY

Received 21 February 2017
Accepted 9 May 2017

KEYWORDS

Molecular dynamics; force fields; metals; minerals; graphite; pH; proteins

1. Introduction

The simulation of organic materials, inorganic materials, biological soft matter and mixed interfaces up to the large nanometer scale helps advance the understanding of energy conversion devices, catalysts, molecular mechanisms of diseases and therapeutics, as well as other functional materials [1–6]. Examples include decorated nanoparticles and nanofillers [7,8], interfaces for charge generation in solar cells [9,10], chemical reactions in batteries [11,12], fuel cells [13], DNA nanotechnology and therapeutics [14,15] and functional nanocomposites [16–18]. Ab-initio calculations are thereby of great help to describe interactions among assemblies of atoms and clusters up to thousands of atoms [19]. Modelling systems up to device scales of 100 nm, the inclusion of solvents and relaxation processes of nanoseconds to microseconds, however, requires classical and reactive molecular dynamics simulations [20,21].

One of the promising approaches for the simulation of inorganic compounds across the periodic table, organic compounds and biomacromolecules is the Interface Force Field (IFF), which

uses the same energy expression as CHARMM, AMBER, PCFF and other major energy expressions (Figure 1) [20]. This paper describes key features, recent advances and opportunities in materials property predictions using this approach. In many instances, interfacial properties can be predicted in same or better accuracy than with DFT methods at 10 million times lower computational cost. Yet there are many areas in which the predictive quality of IFF for new compounds as well as the predictive power of biomolecular force fields such as CHARMM for existing compounds can be improved by several orders of magnitude using Interface parameterisation concepts and protocols.

2. Concepts of the interface approach

The Interface Force Field and surface model database is over 40 inorganic compounds and are in progress to double the coverage in the next release [20]. It has been sufficiently tested for metals, minerals and polymers to achieve coverage across the periodic table in the near future. The initial set of compounds

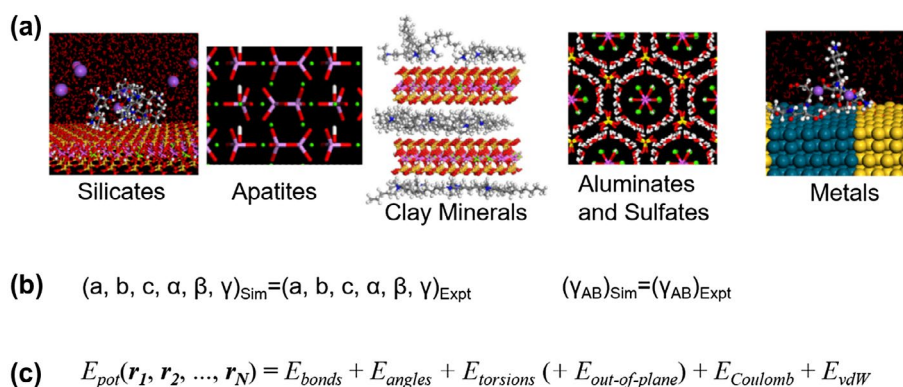


Figure 1. (Colour online) Key aspects of the Interface Force Field (IFF). (a) Representative images of covered compounds, (b) Main features are reproduction of lattice parameters and the surface (or interfacial) energy by the classical Hamiltonian and (c) The potential energy functions are the same as CHARMM, AMBER, GROMACS, PCFF and others to create a uniform simulation platform for all compounds across the periodic table.

Table 1. Atomic charges for selected compounds from experimentally measured electron deformation densities and partition into spherical atomic basins (Hirshfeld method). The values provide a valuable starting point for molecular simulations, especially for polar compounds containing heavy elements. Standard deviations of the last digit are indicated in brackets (see original references in Ref. [20], Table S1).

Compound	Atom	Charge in units of e
LiF	Li	0.95 (3)
LiI	Li	0.67 (5)
LiNO ₂ · H ₂ O	Li(H ₂ O)	0.83
	N	0.51
	O (nitrite)	-0.67
NaCl	Na	1.00 (0)
NaNO ₃ ^a	Na	0.95 (5)
	N	-0.20 (10)
	O	-0.25 (10)
KBr	K	0.8 (1)
CaF ₂	Ca	2.00 (0)
MgO	Mg	1.6 (2)
Al ₂ O ₃	Al	1.32 (5)
AlO(OH)	Al	1.47 (27)
AlPO ₄ ^b	H	0.20 (5)
	Al	1.4 (1)
	P	1.0 (1)
CrSO ₄ · 5 H ₂ O ^c	Cr(H ₂ O) ₅	0.96 (20)
	S	0.24 (6)
	O (sulphate)	-0.30 (6)
Co[O(NC ₅ H ₅) ₆ (ClO ₄) ₂	Co	1.74 (4)
	Cl	-0.12 (1)
	O (perchlorate)	-0.15 (4)
	Pyridine-N-oxide ligand	-0.05 (5) [individual: O -0.83, N 0.27, C ~ -0.2, H ~ 0.3]
CuSO ₄ · 5 H ₂ O ^c	Cu(H ₂ O) ₅	1.18 (10)
	S	0.06 (2)
	O (sulphate)	-0.31 (6)
Cu ₆ Si ₆ O ₁₈ · 6 H ₂ O	Cu	1.23 (6)
	Si	1.17 (15)
	O (water)	-0.74 (6)

Notes: ^aThe density of valence electrons near the middle of the N–O bond is high, leading to an uncertainty in atomic charges up to $\pm 0.1e$; ^bThe crystal structure of AlPO₄ is the same as for tetrahedral SiO₂ (α -quartz) as Al and P are left and right neighbours to Si in the periodic table. The investigation was performed to obtain more information on the charge distribution in the isoelectronic SiO₂, which is non-centrosymmetric and a Si charge of ~ 1.2 was inferred; ^cThe atomic charges are averaged over different environments. Significant anisotropy was observed, such as charge transfer between the metal cation and coordinated water.

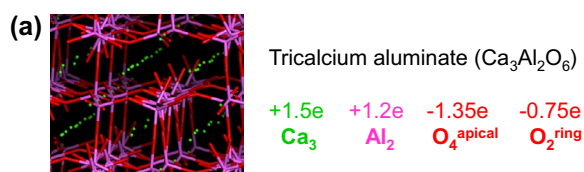
included clay minerals [22], silicates and aluminates [23–25], fcc metals [26], sulphates, phosphates, polyethylene oxide and full consistency with existing parameters for polymers and biomolecules (Figure 1(a)) [27]. The distinction over earlier models for

inorganic compounds, if they were available, is the reproduction of lattice parameters and surface energies in excellent agreement with experiment (Figure 1(b)). Structures and energies are the main quality criteria of a classical (or quantum mechanical) Hamiltonian. Previous force fields, as well as some current force fields, pay no attention to the significance of the energy, either with full neglect or focus on mechanical properties which are the second derivative of the potential energy. Energies such as interfacial energies then often deviate by multiples relative to experimental data [6]. The Hamiltonian can be compatible and chemically realistic only by focus on the structure, energy and secondly on the associated energy derivatives with respect to coordinates and temperature. Therefore, the Interface approach is a generally valid approach to derive force field parameters with full compatibility with existing parameters for other compounds that fulfil the same criteria (e.g. water, organic molecules and other inorganic compounds). The importance and significance of these premises have been confirmed throughout the development for various compounds, and corroborated by further examples on an ongoing basis (see also examples in section 3 below) [6].

To our knowledge, the Interface approach with these foundations is unique and builds on predecessors. The use of the energy expression of existing polynomial force fields (CHARMM, PCFF, GROMACS) leads to broad compatibility, especially for biomacromolecules (Figure 1(c)). Mandatory validation using experimental data provides long-term value, since reproducible experimental data will not change in the future, and removes the dependency on ab initio calculations that suffer from many uncertainties, limitations and scatter. Namely, it is impossible to obtain physically justified atomic charges from DFT [28,29], surface energies of metals by DFT deviate up to 50% from experiment [30], and similar issues for adsorption energies of molecules have been reported [31,32]. These problems are avoided from the outset by full interpretation of parameters in IFF in the context of chemical knowledge and by choosing experimental data as a reference. Deviations in surface energies by 50% as common with DFT methods, for example, have been avoided by application of chemical theory. Therefore, for some systems, the reliability of IFF is an order of magnitude better than DFT methods at the outset and achieves 0 to 10% agreement with experiment for unknown combinatorial interfaces such as DNA/

Table 2. Examples of crystal structures for clay minerals and tobermorite in cement according to X-ray data and NPT molecular dynamics simulation using IFF. The average deviation is less than 0.5%.

Minerals		Cell dim.	<i>a</i> (nm)	<i>b</i> (nm)	<i>c</i> (nm)	α (°)	β (°)	γ (°)	<i>V</i> (nm ³)	rms dev (pm/atom)
Mica	exp	5 × 3 × 1	2.596	2.705	2.005	90	95.73	90	14.00	0
$k_2Si_6Al_6O_{20}(OH)_4$	sim		2.585	2.691	2.006	89.54	95.36	90.01	13.89	15
Pyrophyllite	exp	5 × 3 × 1	2.580	2.690	1.869	91.18	100.46	89.64	12.76	0
$Si_8Al_4O_{20}(OH)_4$	sim		2.589	2.696	1.878	90.62	101.50	90.00	12.84	20
Kaolinite	exp	3 × 2 × 2	1.546	1.788	1.478	91.92	105.04	89.80	3.945	0
$Si_2Al_2O_5(OH)_4$	sim		1.552	1.796	1.464	91.8	104.7	90.06	3.942	26
Tobermorite 11 Å	exp	2 × 2 × 1	1.347	1.477	2.249	90	90	123.25	3.741	0
$Ca_4Si_6O_{15}(OH)_2 \cdot 5H_2O$	sim		1.348	1.467	2.247	89.55	90.15	123.13	3.721	23



(b)

Property	Expt	PCFF	CHARMM	CVFF	AMBER	OPLS-AA
Lattice parameter	1.5263	1.5265	1.5280	1.5240	1.5267	1.5258
<i>a</i> (nm)						
Al–O ^{ring} bond length (pm)	175.5	174.5	174.0	173.5	176.0	175.5
Al–O ^{apical} bond length (pm)	175.0	174.5	172.5	172.0	174.5	174.5
Cleavage energy (mJ/m ²)	1250 ±150 (±12%)	1260 (±0%)	1325 (+5.2%)	1321 (+4.1%)	1341 (+6.4%)	1380 (+9.5%)
Bulk modulus (GPa) at 0-1 GPa	106 ±8	98 ±3	107 ±3	108 ±3	107 ±3	108 ±3

Figure 2. (Colour online) Transferability of parameters and validation of surface and mechanical properties for various polynomial energy expressions for the example of tricalcium aluminate (C3A). (a) Chemical structure and atomic charges and (b) Key structural, energetic and mechanical properties according to experiment and IFF using different energy expressions. Atomic charges are the same in all energy expressions. LJ parameters and/or bonded parameters are slightly adjusted to account for different LJ exponents, combination rules and 1, 4 scaling rules. The performance is closely the same, whereby modulus and cleavage energy are about 5 to 10% lower using a 9-6 LJ potential (PCFF) vs. 12-6 LJ potential (CHARMM, CVFF, AMBER, OPLS-AA). The differences remain within experimental uncertainty. The performance and transferability of IFF for other compounds is similar (adapted with permission from Ref. [24]).

metal, polymer/silica and protein/apatite. Yet it would be incorrect to consider IFF a ‘calibrated’ force field, as numerical fitting is in fact quite minimal. It is also not a ‘boutique’ force field since it can extend to any compound across the periodic table using the same concepts and protocols. IFF is, from its very foundation, a chemically understood force field that provides a molecular code and interpretations for the parameters for each compound included.

A key aspect of the assignment of force field parameters are the atomic charges as they represent the balance between covalent and ionic bonding [28]. Unfortunately, atomic charges have often been misrepresented as numerical fit parameters without chemical rationale. Experimental data from electron deformation densities have been readily available since the 1940’s and systematically disregarded as a reproducible input for molecular simulations (Table 1). The reliability of the near-spherical partition of the electron density of atoms in molecules in the form of atomic charges is about ±0.1e or ±10%, whichever the lower. These data are greatly relevant for molecular simulations as they are consistent with measurements of molecular dipole moments,

physical and chemical properties. These properties need to be represented in molecular dynamics simulations to gain quantitative insight into adsorption, miscibility and chemical reactions. For example, heterolytic bond cleavage, addition and substitution mechanisms in organic chemistry, acid-base equilibria, as well as many other chemical processes and transition state energies require quantitative understanding of local dipole moments that can be represented by atomic charges. When using DFT or higher level QM methods with customary partition schemes, however, the uncertainty in atomic charges for the same compound is often several 100%, effectively useless for classical and reactive MD simulations [6,28,29].

These aspects are so critical, especially for polar inorganic solids, that they are the very basis of the existence of IFF, as it outperforms other approaches by a margin and always permits an explanation of the results obtained. Charge distributions need also not to be limited to atom-centric charges and can include explicit electron configurations such as *d* electrons in metals [33] and π electrons in aromatic rings, especially in newer developments (see Section 3.5). The treatment of atomic charges in IFF,

however, is not entirely based on direct experimental values as often no data are available, and is equally founded in the chemical relationships represented in the Extended Born model [28]. Accordingly, known atomisation energies, ionisation energies, electron affinities, coordination numbers and bond distances provide an equally reproducible rationale for atomic charges, especially relative from one compound to another when a few reference compounds with reliable atomic charges nearby in the periodic table are known. Details of the charge assignments can be found in the original reference and in separate publications introducing force field parameters for specific compounds [20,22–25,27].

A few notable trends from experimental data shown in Table 1 are highlighted in the following. A major observation is that many compounds believed to be ionic are in fact significantly covalent. For example, LiI is best characterised by atomic charges of only $\pm 0.67e$ and not $\pm 1.0e$. Nitrate ions in NaNO_3 have charges of $-0.20e$ on nitrogen and $-0.25e$ on oxygen, very unlike formal charges. Cr in CrSO_4 carries an atomic charge of about $+1.0e$, not a formal charge of $+2.0e$, Al in its oxides and hydroxides about $+1.4e$ and Si in silicates $+1.2e$ (or $+1.1e$), also far from $+4.0e$ assumed in older computational studies [34] or $+2.1e$ in the popular CLAYFF [35]. Since these concepts have not yet been widely applied, much remains to be learned from molecular simulations using realistic polarity. Many inconsistent and erroneous assumptions of atomic charges are still used in molecular simulations and result in highly distorted physical and chemical properties. Interfacial energies, for example, scale with the square of the atomic charges, according to Coulomb's law, and are thus even more strongly affected by discrepancies [22]. Misleading results are often not easily detected in molecular simulations since experimental measurements of the computed target properties may not be immediately feasible, or only properties that are not very energy-sensitive are, in fact, reported. It therefore can take a long time to uncover shortcomings in force fields with sub-par atomic charges. However, unfortunate assumptions about atomic charges will be ultimately dismantled after some time as they lead to inevitable disagreements of major scale. Therefore, it is worth making informed choices of atomic charges from the start based on experimental evidence, the Extended Born model, and chemical cross-checks, as earlier described [6,20,28], and not on ab initio calculations, to prevent unnecessary confusion and nonsensical results.

One of the earliest examples showing the relevance of experimental data for atomic charges, in sharp contrast to ab initio calculations, are the common SPC and TIP5P water models in the 1980s [36,37]. Atomic charges according to experimental dipole moments for liquid and gas phase water were used in these force fields, and not speculative, widely scattered charges from ab initio calculations, which offer a whopping range from $-0.17e$ to $-1.24e$ for O atoms [28]. For example, the SPC water model employs an O charge of $-0.82e$, very close to the result from electron deformation density measurements in a hydrous copper silicate of $-0.74e$ (Table 1). While it is not possible to determine unequivocal 'exact' atomic charges, the typical uncertainty is only 10% (using multiple measures: 5%) and therefore the room to freely choose one particularly well performing value very limited.

IFF reproduces lattice parameters for a range of complex inorganic and hydrous minerals, shown for some representative examples (Table 2). On average, the lattice constants deviate less than 0.5% from X-ray data and the number of force field types is small. In the IFF parameterisation, the second step after assigning atomic charges is the assessment of covalent bonding terms between pairs of nearest atoms. Terms for covalent bonding are assigned if the average atomic charges are less than half the formal charges. If atomic charges between pairs of nearest atoms are more than half the formal charges, no explicit bonding terms are necessary, i.e. Coulomb plus Lennard-Jones parameters suffice. The bonded terms include harmonic bond stretching and angle bending functions, plus torsion and out of plane for chain molecules and planar molecules depending on need, consistent with the functional form of CHARMM, PCFF and other force fields. Next follows the final definition of atom types (initial atom types are identified along with the analysis of the structure and charges), at least one per element and often more depending on chemical environment to specify separate Lennard-Jones parameters in different chemical environments and particular bond angles, for example. Using an available crystal structure from X-ray data, the initial bond lengths and bond angles are defined, as well as harmonic stretching constants according to experimental IR spectra and computed velocity autocorrelation functions. The assignment of initial Lennard-Jones parameters follows established trends across the periodic table (see Refs. [6,20]). Lattice parameters are computed with all atoms flexible in NPT molecular dynamics and refinements of the parameters made to match the X-ray data ($<0.1\%$ deviation if possible). Subsequently, an appropriate energy, e.g. cleavage energy, hydration energy, is computed and compared to available experimental measurements, followed by adjustments in Lennard-Jones and bonded parameters to reproduce this energy ($<1\%$ uncertainty if possible). Last, secondary checks of elastic constants, heat capacity, thermal expansion and other derivative properties can be carried out, which typically do not require further adjustments of parameters. The concept of reproducing atomic charges (the nature of chemical bonding), structures and energies first typically means that all other properties follow as good as possible without further need for parameter adjustments thereafter. The force field parameters are then also interpreted in the context of similar compounds, which helps in refinements during the above optimisation, and finally locked in similar to a molecular code for the given compound.

The transferability of parameters from one to another harmonic/polynomial energy expression is very good. In some cases, such as Lennard-Jones (LJ) parameters for fcc metals with zero atomic charge [26], it is even trivial. In other instances, atomic charges remain the same for every energy expression and adjustments in LJ parameters are made to accommodate the different functional form (e.g. 9-6 vs. 12-6 LJ parameters), combination rules and scaling of non-bond interactions between 1,4 bonded atoms. The compatibility and transferability is illustrated for tricalcium aluminate using different energy expressions with appropriately modified parameters (Figure 2(a) and (b)). Only minor differences in computed properties are seen. Lattice parameters and bond lengths are essentially identical. Differences of 0.1% in lattice parameters and up to 1% in individual bond lengths are tolerable. Cleavage energies as the major energy criterion for

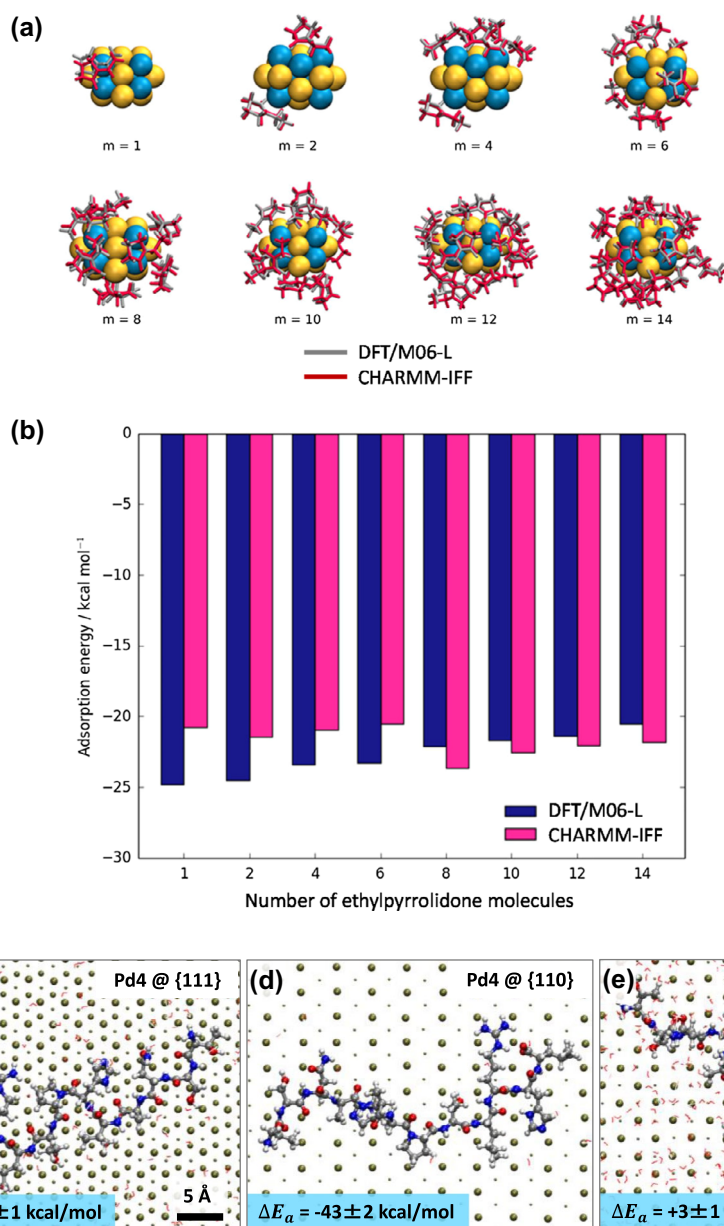


Figure 3. (Colour online) Equilibrium conformations and binding energies of organic ligands adsorbed on small AuPd nanoparticles using DFT and CHARMM-IFF, as well as facet specific differences of the adsorption of a peptide on (hkl) metal facets in aqueous solution using CHARMM-IFF. (a) AuPd nanoparticles in contact with ethylpyrrolidone for various surface coverage using DFT and CHARMM-IFF (reproduced with permission from Ref. [51]), (b) Computed adsorption energies using DFT and CHARMM-IFF. The agreement is excellent and the computational expense is ten million times lower using CHARMM-IFF (reproduced with permission from Ref. [51]) and (c–e) Distinct binding patterns and adsorption energies of the Pd4 peptide (TSNAVHPTLRHL) on (hkl) surfaces of palladium in water at pH ~ 7 computed by CHARMM-IFF. The trends in adsorption strength (111) > (110) > (100) are similarly observed for other peptide sequences, ligands and fcc metal surfaces related to a soft epitaxial binding mechanism.

validation are within the experimental uncertainty of $\pm 12\%$ for all energy expressions, and tend to be 5% to 10% higher using 12-6 LJ potentials (CHARMM, CVFF, AMBER, OPLS-AA) compared to the 9-6 LJ potential (PCFF). The origin for these changes is stronger repulsion in the 12-6 LJ potentials, especially as non-bond interactions between 1,4 bonded atoms are partially excluded (full inclusion of Coulomb and LJ interactions in CHARMM/CVFF vs. 83.3/50% inclusion in AMBER and 50/50% inclusion in OPLS-AA). Other properties such as bulk and Young's modulus agree very well with experiment without further adjustments (Figure 2(b)) [24], in part compensating the deviation in cleavage energy for tricalcium aluminate.

3. Insight into molecular recognition on surfaces, nanoparticles and surface reactions

3.1. Metal–organic interfaces

Metal–water and metal–organic interfaces can be very precisely understood using IFF due to the representation of surface and interfacial energies with uncertainties in the low per cent range [26]. The models and simulations indeed allowed the discovery of the mechanism of non-covalent ligand binding to metal surfaces consistent with experiment, which involves attraction of polarisable atoms (C, N, O, S) to epitaxial sites on the metal surface [38]. Details and implications of this mechanism, specific

guidance in nanocrystal growth and catalytic performance have since then been elucidated [39–45]. Specific peptide sequences for shape control in synthesis [46,47] and nanoparticle shapes for higher reactivity in catalysis were suggested [48,49]. IFF has also been used as a reactive force field by allowing bond breaking and computation of transition state energies in the form of activation energies and proxies thereof [48–50]. The advantage over DFT calculations to assess reaction rates is access to much larger system size, full inclusion of solvents and large molecular ligands, pH conditions and extensive dynamics at low computational cost.

Recently, a direct comparison of the conformations and adsorption energies of ethylpyrrolidone to small AuPd nanoparticles was reported using DFT at the M06 level and molecular mechanics using CHARMM-IFF, which demonstrates quantitative agreement (Figure 3(a) and (b)) [51]. The conformations of the adsorbed molecules for a set of different surface coverage have an excellent degree of match (Figure 3(a)). The adsorption energies agree within 10% or better, which is also a remarkable fit (Figure 3(b)). The data also do not signify that DFT would be more accurate than CHARMM-IFF as surface energies of metals from DFT deviate much more from experiment (up to 50%) than with IFF (typical uncertainty <5%) [30]. Nevertheless, the data clearly show that it is not necessary to use DFT or ab initio dynamics for equilibration and conformation analysis. The much more expensive quantum mechanical calculations can be restricted to the investigate local electron densities and stereoelectronic effects pertinent to surface reactions. Rate predictions for large series of catalysts, for example, can be carried out using a combination of chemical knowledge of reaction mechanisms, DFT, QM/MM calculations and reactive molecular dynamics using reactive modifications of IFF or ReaxFF.

An example of differential binding of larger organic ligands to (hkl) metal surfaces in aqueous solution is shown for a palladium-binding peptide TSNAVHPTLRHL [52] on (1 1 1), (1 1 0) and (1 0 0) surfaces of palladium metal (Figure 3(c)–(e)). The conformations and energies were obtained using CHARMM-IFF [20]. The metal surface is depicted with larger spheres for atoms in the top layer, medium spheres for atoms in the first sublayer, and yet smaller spheres for atoms in the second sublayer (following the ABCABC stacking sequence of fcc Pd metal). On the (1 1 1) surfaces that show the full ABC stacking sequence, the coordination of epitaxial sites (sublayer sites) by the peptide is clearly seen (Figure 3(c)). The backbone and the side chains adapt conformations that avoid contact with top layer atoms and coordinate a maximum of polarisable atoms (C, N, O) with hollow sites. In these conformations, the peptide binds stronger to the surface than competing water molecules and achieves the most attractive adsorption energy of –68 kcal/mol among all facets. Very significant adsorption is also found on (1 1 0) facets, although the wider grooves in the surface reduce the specificity of adsorption (Figure 3(d)). Several side chains orient themselves parallel to the wide grooves, gaining access to epitaxial sites. The overall selectivity of adsorption of the Pd4 peptide versus water is not as strong as on the (1 1 1) surface, leading to somewhat diminished attraction with –43 kcal/mol adsorption energy. Finally, on the (1 0 0) surface, water adsorbs more strongly and the peptide has barely any surface contact (Figure 3(e)). The square pattern of epitaxial sites at 2.75 Å distance is very difficult

to match by polarisable atoms in the chain molecule, resulting in stronger coordination of epitaxial sites by small mobile water molecules and in a water interlayer between the metal surface and the peptide (side view not shown). Therefore, the adsorption energy turns slightly positive to +3 kcal/mol.

These facet-specific trends for adsorption, i.e. stronger adsorption in the order (1 1 1) > (1 1 0) > (1 0 0), are similarly found for other peptide sequences, ligands and synthetic polymers [38,41,42,44]. Differences according to monomer sequence and chemistry are observed, although rarely strong enough to supercede the classification according to facet (Figure 3(c)–(e)). Facet-specific trends are also similar for other fcc metals such as Ag, Al, Au, Cu, Ni, Pt and Rh. The relative strength of adsorption is proportional to the surface energy (ranging from 1.2 to 2.5 J/m² with 1.98 J/m² for Pd) [26,53], and the extent of binding differential to distinct (hkl) facets is also proportional to the surface energy [6]. A particular case is the binding of thiols, however, which leads to stronger adsorption via multi-centre covalent bonds, and needs a bonded approximation in IFF (using a larger LJ well depth for the chemically bonded S atom) [50,54].

3.2. Surface properties of pH-sensitive mineral surfaces and selective adsorption of biomolecules

The surface chemistry of minerals such as silica, carbonates and phosphates is greatly dependent on pH [55–57]. Large changes in cleavage energies, hydration energies and adsorption equilibria are known experimentally and have recently been introduced into surface models supplied with IFF (Figure 4) [20]. Information on the surface chemistry of minerals can be obtained using experimental pK values of the corresponding acids, measurements of the zeta potential and point of zero charge, in a very detailed fashion from surface titration, as well as from spectroscopy of the surfaces [23,58]. Interestingly, quantitative, reproducible data have been available for over 50 years yet for the first time systematically incorporated into molecular models and molecular simulations in IFF. There are no alternatives to using experimental data, too, as ab initio calculations cannot be applied to the required large systems with many water molecules, ionic concentrations and dynamics. Ab-initio methods are also of limited reliability to predict pK values and pH equilibria. Experimental data, once measured reproducibly, have the advantage of high accuracy and permanent validity, unlike continuous changes in density functionals where it is hardly certain which functional and which value to trust.

A useful future step in building pH resolved models for compounds like silica, titania, apatites, carbonates and other oxides will be the development of a graphical user interface that automatically generates models of (hkl) surfaces and nanostructures of correct surface chemistry, using all known experimental data. The relevance of correct surface models is high as it has been shown, for example, that combinatorially selected peptides binding to ordinary silica at pH 3 have less than 10% sequence similarity with peptides binding to the same silica at pH 7 [57,59]. The same lack of correlation is found when a different type of silica, e.g. Q² rather than Q³ silica is used. Many computational studies with unrealistic assumptions of surface chemistry have been published at DFT and MD levels that have poor credibility [6]. Common unrealistic assumptions include non-protonated

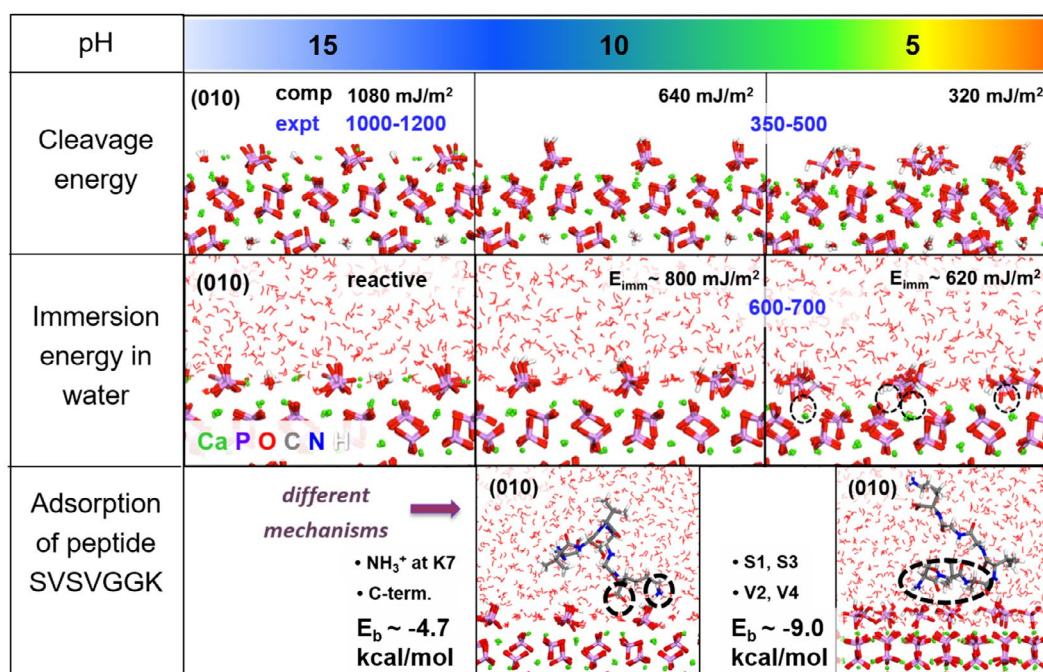


Figure 4. (Colour online) pH responsive surfaces of hydroxyapatite (HAP) and selective peptide adsorption. Cleavage and hydration (immersion) energies change remarkably for different solution acidity, related to modifications in the density of superficial calcium ions and protonated phosphate ions. Changes in binding mechanism from ion pairing at higher pH towards weaker ion pairing and hydrogen bonds at lower pH affect the selective adsorption of peptides, binding residues and binding energy as shown for the HAP-binding peptide SVSVGK (adapted from Ref. [27] with permission).

hydroxyapatite and calcium carbonate surfaces at pH 7, silica surfaces without silanol groups or inappropriate surface ionisation, non-protonated titania surfaces, or entirely non-stoichiometric surfaces, and without mention of possible differences in surface chemistry and pH equilibria. The use of realistic surface models and force fields can enormously improve the fidelity of molecular dynamics simulations to gain insights into mineralisation/demineralisation, surface reactions and biological calcification, placing molecular simulations closer to par with experimental measurements [59]. Computed binding free energies of peptides to various silica surfaces, for example, have reached $\pm 10\%$ agreement with laboratory measurements [59].

Hydroxyapatite, as a recent example, is among the most important biominerals in bone and teeth (Figure 4). The surface energies for the dominant (010) basal plane change from 1080 to 320 mJ/m² as protonation proceeds from the neat cleaved hydroxy phosphate surfaces that are only stable at pH values >15 to physiological pH values of ~5 in bone (Figure 4) [27]. The highly adaptive surface states are critical for reversible crystal growth and dissolution. The hydration energy (immersion energy) also changes from values above 1000 mJ/m² at pH 15 to 800 mJ/m² at pH 10 and ~620 mJ/m² at pH 5. The accompanying decrease in area density of calcium ions on the surface leads to different adsorption mechanisms of peptides and proteins (Figure 4). The area density of calcium ions is about half for dihydrogen phosphate termination at pH 5 compared to that for monohydrogen phosphate termination of the hydroxyapatite surface at pH 10. Higher pH values of ~10 lead to ion pairing between the carboxylate anion of the C terminus of the peptide SVSVGK and superficial calcium ions on the apatite surface, as well as between the ammonium group of the lysine side chain (only partially protonated above pH 9) with negatively charged

oxygen atoms in superficial monohydrogenphosphate ions. At lower pH values of ~5, binding residues change to serine and valine, which form hydrogen bonds with dihydrogen phosphate surface groups. An ion pair remains between the N-terminal ammonium group and surface anions, and the overall adsorption energy at pH ~5 can be stronger than at pH ~10. The recognition mechanisms of peptides therefore shift significantly on apatites as a function of solution conditions, and simulations tools are ready to identify biochemical implications [27].

3.3. Defects and strain fields in alloys

The application of pair potentials to metals is still a recent development and consistent with quantum mechanical descriptions of pairwise interatomic interactions rather than artificial many body interactions [26]. Bcc metals such as tungsten and iron can be described using extensions of the single atom Lennard-Jones potential with four virtual *d* electrons of negative charge. The potential then employs harmonic W–e bonds, e–W–e angles, Coulomb and van-der-Waals interactions [33]. The coverage of multiple bcc, hcp and fcc metals using this approach is in progress and enables precise reproduction of crystal structure, surface energy, as well as elastic constants.

The first of these potentials for W was developed along with parameters for occluded C to quantify the diffusion of carbon atoms into a tungsten tip (forming WC_x), coupled with experimental measurements to explain the observed strain tensor and elucidate the likely depth of penetration of carbon atoms (Figure 5) [33]. The experimental measurement was performed by atomic electron tomography (AET), allowing 3D structure determination of crystals defects and chemical order/disorder of materials at atomic resolution [60–63]. Figure 5(a) shows the

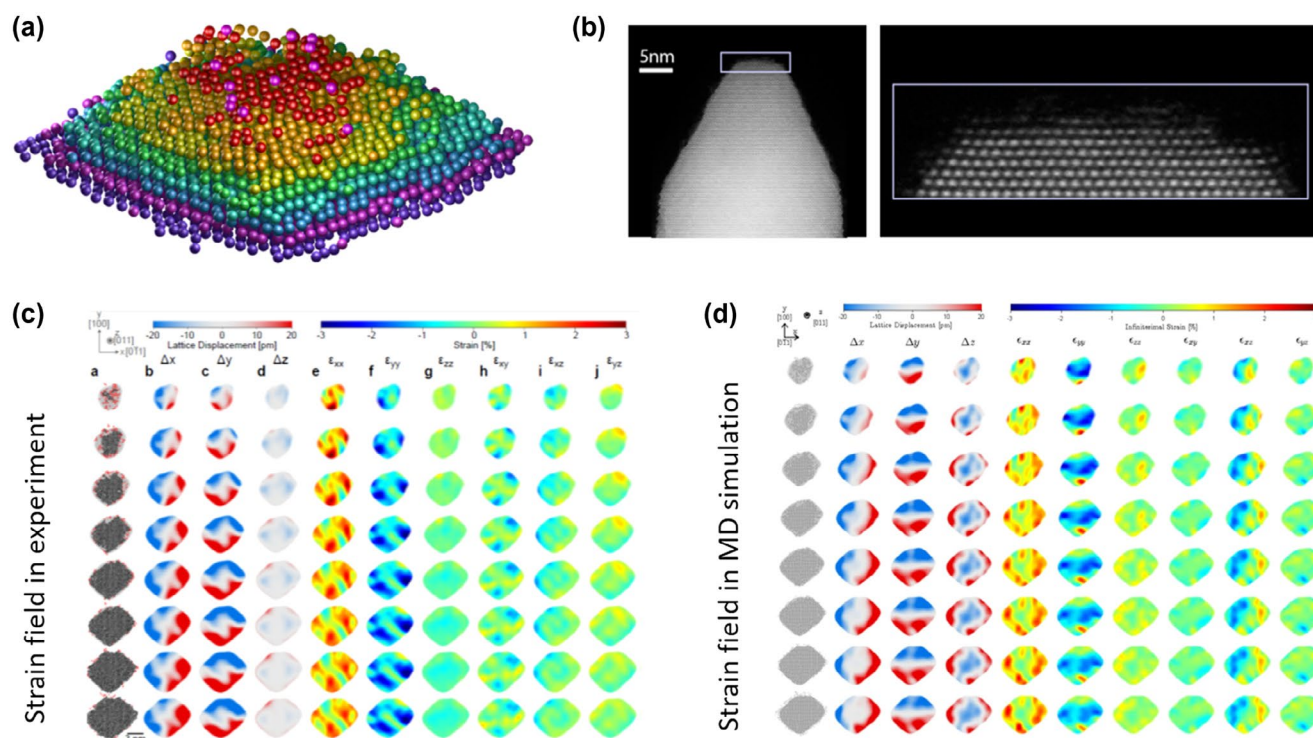
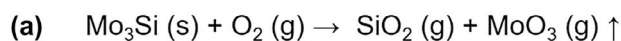
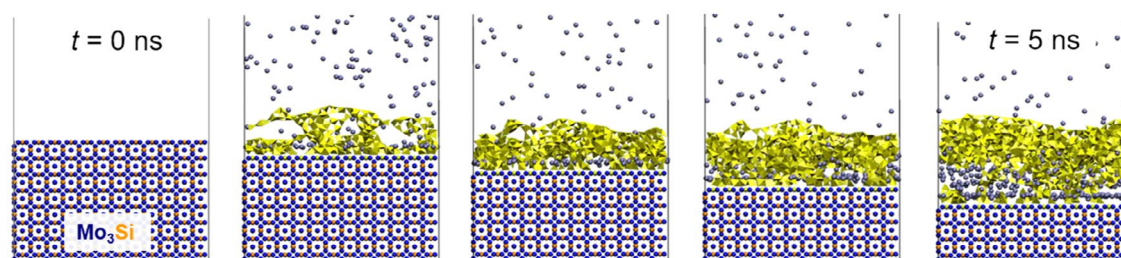


Figure 5. (Colour online) Structure and strain field of a WC_x tip in experiment and simulation. (a) 3D structure of a WC_x tip that contains amorphous carbon inclusions. The positions of the W atoms are shown according to atomically resolved electron tomography, colored by atomic layer. The positions of carbon atoms that cause disorder cannot be seen, (b) Transmission electron micrograph of the sample using the TEAM I microscope (one projection). Occluded carbon atoms weakened the intensity or appear as invisible dark spots, (c) The strain field in each atomic layer according to experiment and (d) The computed strain field in each atomic layer after insertion of carbon atoms with a reasonably close match to experiment. The carbon atoms penetrate into the W tip 8 atomic layers with a surface composition of approximately WC_{0.15} (reproduced with permission from Ref. [33]).



(b)

Mo Si MoO₃ SiO₂



(c)

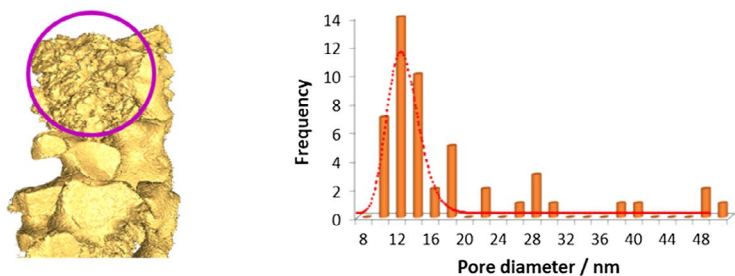


Figure 6. (Colour online) Reactive molecular dynamics simulation of Mo₃Si oxidation using IFF and related experimental data. (a) Reaction scheme, (b) Formation of a protective amorphous, porous silica layer as a function of simulation time on the Mo₃Si alloy surface at 800 °C monitored by reactive MD. The evaporation of MoO₃ can be seen (gray spheres) and (c) Morphology of porous silica structures after complete oxidation of samples in experiment, analysed by equal slope tomography (about 100 nm size). The sample shows smaller porosity (circled, top), higher porosity (bottom) and the pore size distributions can be broad (plot on the right).

3D atomic positions of the W tip with 19 pm precision. The observed irregularity of the surface structure is related to the inclusion of C atoms, which cannot be detected in the electron microscope. The projection from the side view also shows gaps and overall lower definition of atomic positions in the superficial atomic layers of the tungsten tip (Figure 5(b)). To determine the

approximate location of unidentified carbon atoms, molecular dynamics simulations with different carbon loading and distribution were carried out. For each equilibrium structure, the strain fields of the tungsten atoms relative to a perfect bcc lattice were computed and compared with the strain field according to experiment (Figure 5(c) and (d)). As a result, the surface

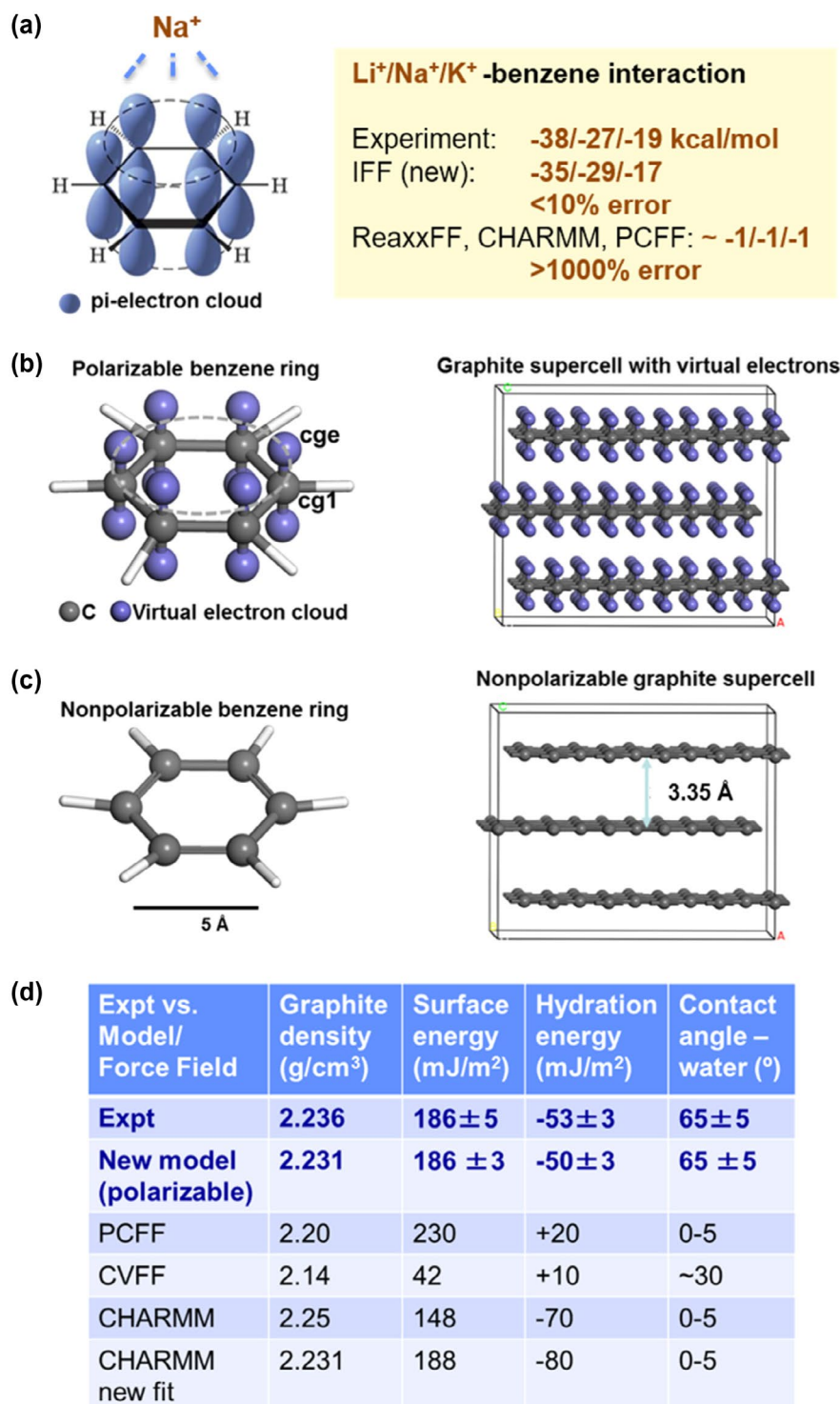


Figure 7. (Colour online) New IFF models for graphitic and π -conjugated molecules with virtual electrons to account for cation- π , π - π stacking, H- π bonds, solvent and organic interactions. (a) The magnitude of cation- π interactions is far greater than hydrogen bonds and neglected in prior force fields, (b) New models with virtual π electrons overcome this problem quantitatively, (c) Existing models exclude local Coulomb interactions that are essential for the interfacial dynamics of π -conjugated molecules and graphitic layers and (d) Density, surface energy, hydration energy and contact angle of graphite according to experiment, the new graphitic force field and existing force fields. Large deviations in hydration energies and contact angles are removed. Force fields for many aromatic compounds, including DNA, amino acids and polymer semiconductors can greatly benefit from analogous refinements to include virtual π electrons.

composition was found to be approximately $WC_{0.15}$ and the penetration depth of carbon atoms amounted to about eight atomic layers [33]. The example shows that high resolution imaging can be well combined with molecular simulations to quantify missing structural details and explain observed properties. An essential part of such modelling is the construction of models that closely match the experimental system, which can be challenging in details.

3.4. Reactive molecular dynamics of alloy oxidation

Mo-Si-B alloys are used for the protection of SiC-C composites and ultrahigh temperature applications [64,65]. The oxidation at temperatures above 800 °C involves the formation of an amorphous silica layer that possesses a porous structure and protects the alloy from further oxidation once a certain thickness is reached (Figure 6(a)) [66]. To understand details of the oxidation mechanism for the neat Mo_3Si (A15) alloy, reactive molecular dynamics simulations were employed, in which the crystalline Mo_3Si was oxidised layer-by-layer at a given rate, producing MoO_3 gas and silica (Figure 6(b)). The formed silica was described by a non-bonded potential (Coulomb plus LJ) that reproduces bond geometry, density and modulus. Nascent MoO_3 gas was represented by coarse-grain beads that reproduce the molecular volume and intermolecular interactions (Lennard-Jones parameters σ and ϵ). The morphology of the developing porous silica layer varies as a function of temperature and oxygen partial pressure. Thin layers (2 nm) have less porosity than layers grown beyond 100 nm thickness as observed using equal slope tomography (Figure 6(c)) [67]. Qualitative trends in pore size as a function of temperature and oxidation rate from the simulation correlate with experimental observations and will be later reported in detail. The computational protocol can be applied up to millions of atoms to study the formation and properties of amorphous oxide layers.

3.5. New models for graphitic materials and π -conjugated molecules

New models for graphitic materials and π -conjugated molecules have been developed as part of IFF (Figure 7). The inclusion of virtual π electrons addresses a fundamental shortcoming in existing all-atom force fields - the neglect of internal polarity of conjugated systems that account for cation- π and π - π -stacking interactions (Figure 7(a)) [68–70]. These interactions amount nearly to the strength of weak covalent bonds and are about 100 times stronger than computed by current force fields such as CHARMM, CVFF, AMBER and ReaxFF. The new models include virtual electrons via harmonic bond and angle terms that reproduce the strength of cation- π interactions measured in experiment (Figure 7(b)). Therefore, multipoles along the cloud of conjugated π -electrons are represented truthfully. The atomic charges are +1e on each aromatic carbon atom and -0.5e on the two corresponding virtual electron clouds above and below the atomic plane. Traditional force fields take no note of these interactions (Figure 7(c)) and lead to large errors in computed cation- π interactions, surface energies, hydration energies and contact angles with solvents (Figure 7(d)). The registry of

graphitic layer stacking is also reproduced with the new models, while challenging with the older models. The computed density and surface energy are in much better agreement with experiment. The enhancements in the representation of interactions of graphitic substrates with water, organic and biological macromolecules are critical as such interactions are qualitatively misleading when neat LJ potentials without charges for the π electrons are used (Figure 7(d)). Hydration energies have sometimes been obtained positive rather than negative, and contact angles very far from experimental observations without these new additions. Clearly, LJ parameters alone are a poor approximation for non-bond interactions between graphitic layers and can be very much improved.

The concept of this treatment also applies to aromatic molecules such as benzene, DNA bases, aromatic amino acids (Phe, Tyr, Trp, His) and conjugated polymers. Very similar parameters can be used, with superposition of added polarity by heteroatoms, to significantly improve predictions of stacking of DNA bases, CH- π bonds and include realistic ion effects. The same enhancements apply to conjugated polymers for solar cells and displays such as polythiophenes (e.g. P3HT) and paraphenylene vinylenes (PPVs) to describe polymer folding and morphology more reliably. The introduction of virtual π electrons will also enable a revision of standard biological force fields and organic force fields (CHARMM, AMBER, GROMACS, OPLS-AA, PCFF). On this path, the Interface concept will maintain full compatibility with existing parameters also after virtual electrons are added as a result of thorough validation of chemical bonding, structure and energies for each compound. This is a great advantage as therefore no re-parameterisation of other compounds or functional groups will be required.

4. Conclusions

Concepts and recent progress in the simulation of inorganic and biological-inorganic hybrid interfaces using the Interface MD platform have been summarised. IFF relies on a universal procedure to determine force field parameters based on chemically justified charges, validation of structures and energies for each compound using reproducible experimental data rather than ab initio computed quantities subject to ongoing amendments. The most common harmonic/polynomial energy expressions are used to accommodate compounds across the periodic table for predictions in high accuracy using a single simulation platform.

Interfaces of metal nanostructures with organic molecules and biopolymers can be simulated in the same accuracy as with DFT methods at far lower computational cost. Interfaces of oxides, hydroxides, phosphates, silicates and other minerals with water and ligands can be simulated in quantitative agreement with experiment for surface chemistries consistent with pH and ionic strength. Recent applications to alloys, including bcc metals, and reactive molecular dynamics using IFF were illustrated that provide insight into surface reactions and morphology development upon oxidation and corrosion. New representations of π electron density are described to correctly include multipole moments, cation- π interactions and polarity of graphitic substrates upon interaction with water, polar molecules and ionic macromolecules.

Acknowledgements

JM acknowledges the help from M. Taylor, J. Perepezko and G. A. Melinte. The allocation of computational resources at the CU Biofrontiers Computing Cluster and at the Ohio Supercomputing Center is acknowledged.

Disclosure statement

No potential conflict of interest was reported by the authors.

Funding

This work was supported by the National Science Foundation, under Division of Chemical, Bioengineering, Environmental, and Transport Systems [grant number CBET-1530790], under Division of Materials Research [grant number DMR-1548924], [grant number DMR-1437263], and [grant number DMREF-1623947]; Air Force Office of Scientific Research (AFOSR) [grant number FA9550-14-1-0194]; Office of Naval Research ONR-MURI [grant number N00014-14-1-0675]; American Chemical Society Petroleum Research Fund ACS-PRF [grant number 54135-ND10]; the Oak Ridge Leadership Computing Facility at the Oak Ridge National Laboratory, which is supported by the Office of Science of the U.S. Department of Energy [contract number DE-AC05-00OR22725]; the Argonne Leadership Computing Facility, which is a DOE Office of Science User Facility supported [contract number DE-AC02-06CH11357]; and the Janus supercomputer, which is supported by the National Science Foundation [grant number CNS-0821794].

References

- Li MF, Zhao ZP, Cheng T, et al. Ultrafine jagged platinum nanowires enable ultrahigh mass activity for the oxygen reduction reaction. *Science*. 2016;354:1414–1419.
- Smeets PJM, Cho KR, Kempen RGE, et al. Calcium carbonate nucleation driven by ion binding in a biomimetic matrix revealed by in situ electron microscopy. *Nat Mater*. 2015;14:394–399.
- Bonaccorso F, Colombo L, Yu G, et al. Graphene, related two-dimensional crystals, and hybrid systems for energy conversion and storage. *Science*. 2015;347, 1246501.
- Wegst UGK, Bai H, Saiz E, et al. Bioinspired structural materials. *Nat Mater*. 2015;14:23–36.
- Nicolosi V, Chhowalla M, Kanatzidis MG, et al. Liquid exfoliation of layered materials. *Science*. 2013;340:1226419.
- Heinz H, Ramezani-Dakhl H. Simulations of inorganic–bioorganic interfaces to discover new materials: insights, comparisons to experiment, challenges, and opportunities. *Chem Soc Rev*. 2016;45:412–448.
- Dreaden EC, Alkilany AM, Huang XH, et al. The golden age: gold nanoparticles for biomedicine. *Chem Soc Rev*. 2012;41:2740–2779.
- Heinz H, Pramanik C, Heinz O, et al. Nanoparticle decoration with surfactants: molecular interactions, assembly, and applications. *Surf Sci Rep*. 2017;72:1–58.
- Jeon NJ, Noh JH, Yang WS, et al. Compositional engineering of perovskite materials for high-performance solar cells. *Nature*. 2015;517:476–480.
- Liu H, Espe M, Modarelli DA, et al. Interaction of substituted poly(phenyleneethynylene)s with ligand-stabilized CdS nanoparticles. *J Mater Chem A*. 2014;2:8705–8711.
- Xu J, Wu J, Luo L, et al. Co₃O₄ nanocubes homogeneously assembled on few-layer graphene for high energy density lithium-ion batteries. *J Power Sources*. 2015;274:816–822.
- Kirklin S, Meredig B, Wolverton C. High-throughput computational screening of new Li-ion battery anode materials. *Adv Energy Mater*. 2013;3:252–262.
- Huang XQ, Zhao ZP, Cao L, et al. High-performance transition metal-doped Pt₃Ni octahedra for oxygen reduction reaction. *Science*. 2015;348:1230–1234.
- Auyeung E, Morris W, Mondloch JE, et al. Controlling structure and porosity in catalytic nanoparticle superlattices with DNA. *J Am Chem Soc*. 2015;137:1658–1662.
- Sun M, Yang C, Zheng J, et al. Enhanced efficacy of chemotherapy for breast cancer stem cells by simultaneous suppression of multidrug resistance and antiapoptotic cellular defense. *Acta Biomater*. 2015;28:171–182.
- Suter JL, Groen D, Coveney PV. Chemically specific multiscale modeling of clay-polymer nanocomposites reveals intercalation dynamics, tactoid self-assembly and emergent materials properties. *Adv Mater*. 2015;27:966–984.
- Kaushik A, Kumar R, Arya SK, et al. Organic-inorganic hybrid nanocomposite-based gas sensors for environmental monitoring. *Chem Rev*. 2015;115:4571–4606. Epub 2015 May 02.
- Fu YT, Heinz H. Cleavage energy of alkylammonium-modified montmorillonite and relation to exfoliation in nanocomposites: Influence of cation density, head group structure, and chain length. *Chem Mater*. 2010;22:1595–1605.
- Booth GH, Grueneis A, Kresse G, et al. Towards an exact description of electronic wavefunctions in real solids. *Nature*. 2013;493:365–370.
- Heinz H, Lin T-J, Mishra RK, et al. Thermodynamically consistent force fields for the assembly of inorganic, organic, and biological nanostructures: the interface force field. *Langmuir*. 2013;29:1754–1765.
- Chenoweth K, van Duin ACT, Goddard WA. ReaxFF reactive force field for molecular dynamics simulations of hydrocarbon oxidation. *J Phys Chem A*. 2008;112:1040–1053.
- Heinz H, Koerner H, Anderson KL, et al. Force field for mica-type silicates and dynamics of octadecylammonium chains grafted to montmorillonite. *Chem Mater*. 2005;17:5658–5669.
- Emami FS, Puddu V, Berry RJ, et al. Force field and a surface model database for silica to simulate interfacial properties in atomic resolution. *Chem Mater*. 2014;26:2647–2658.
- Mishra RK, Fernández-Carrasco L, Flatt RJ, et al. A force field for tricalcium aluminate to characterize surface properties, initial hydration, and organically modified interfaces in atomic resolution. *Dalton Trans*. 2014;43:10602–10616.
- Mishra RK, Flatt RJ, Heinz H. Force field for tricalcium silicate and insight into nanoscale properties: cleavage, initial hydration, and adsorption of organic molecules. *J Phys Chem C*. 2013;117:10417–10432.
- Heinz H, Vaia RA, Farmer BL, et al. Accurate simulation of surfaces and interfaces of face-centered cubic metals using 12–6 and 9–6 Lennard-Jones potentials. *J Phys Chem C*. 2008;112:17281–17290.
- Lin TZ, Heinz H. Accurate force field parameters and pH resolved surface models for hydroxyapatite to understand structure, mechanics, hydration, and biological interfaces. *J Phys Chem C*. 2016;120:4975–4992.
- Heinz H, Suter UW. Atomic charges for classical simulations of polar systems. *J Phys Chem B*. 2004;108:18341–18352.
- Gross KC, Seybold PG, Hadad CM. Comparison of different atomic charge schemes for predicting pKa variations in substituted anilines and phenols. *Int J Quantum Chem*. 2002;90:445–458.
- Singh-Miller NE, Marzari N. Surface energies, work functions, and surface relaxations of low-index metallic surfaces from first principles. *Phys Rev B*. 2009;80:235407.
- Valero R, Gomes JR, Truhlar DG, et al. Density functional study of CO and NO adsorption on Ni-doped MgO(100). *J Chem Phys*. 2010;132:104701. Epub 2010 Mar 18.
- Zhao Y, Truhlar D. The M06 suite of density functionals for main group thermochemistry, thermochemical kinetics, noncovalent interactions, excited states, and transition elements: two new functionals and systematic testing of four M06-class functionals and 12 other functionals. *Theoret Chem Acc*. 2008;120:215–241.
- Xu R, Chen C-C, Wu L, et al. Three-dimensional coordinates of individual atoms in materials revealed by electron tomography. *Nat Mater*. 2015;14:1099–1103.
- Sanders MJ, Leslie M, Catlow CRA. Interatomic potentials for SiO₂. *J Chem Soc-Chem Commun*. 1984:1271–1273.
- Cygan RT, Liang J-J, Kalinichev AG. Molecular models of hydroxide, oxyhydroxide, and clay phases and the development of a general force field. *J Phys Chem B*. 2004;108:1255–1266.

- [36] Berendsen HJC, Grigera JR, Straatsma TP. The missing term in effective pair potentials. *J Phys Chem.* **1987**;91:6269–6271.
- [37] Mahoney MW, Jorgensen WL. A five-site model for liquid water and the reproduction of the density anomaly by rigid, Nonpolarizable Potential Functions. *J Chem Phys.* **2000**;112:8910–8922.
- [38] Heinz H, Farmer BL, Pandey RB, et al. Nature of molecular interactions of peptides with gold, palladium, and Pd-Au bimetal surfaces in aqueous solution. *J Am Chem Soc.* **2009**;131:9704–9714.
- [39] Coppage R, Slocik JM, Briggs BD, et al. Crystallographic recognition controls peptide binding for bio-based nanomaterials. *J Am Chem Soc.* **2011**;133:12346–12349.
- [40] Heinz H, Jha KC, Luettmer-Strathmann J, et al. Polarization at metal-biomolecular interfaces in solution. *J R Soc Interface.* **2011**;8:220–232. Epub 2010/07/16.
- [41] Jha KC, Liu H, Bockstaller MR, et al. Facet recognition and molecular ordering of ionic liquids on metal surfaces. *J Phys Chem C.* **2013**;117:25969–25981.
- [42] Feng J, Pandey RB, Berry RJ, et al. Adsorption mechanism of single amino acid and surfactant molecules to Au 111 surfaces in aqueous solution: design rules for metal-binding molecules. *Soft Matter.* **2011**;7:2113–2120.
- [43] Feng J, Slocik JM, Sarikaya M, et al. Influence of the shape of nanostructured metal surfaces on adsorption of single peptide molecules in aqueous solution. *Small.* **2012**;8:1049–1059.
- [44] Ramezani-Dakhel H, Ruan LY, Huang Y, et al. Molecular mechanism of specific recognition of cubic Pt nanocrystals by peptides and the concentration-dependent formation from seed crystals. *Adv Func Mater.* **2015**;25:1374–1384.
- [45] Briggs B, Bedford N, Seifert S, et al. Atomic-scale identification of Pd leaching in nanoparticle catalyzed CC coupling: effects of particle surface disorder. *Chem Sci.* **2015**;6:6413–6419.
- [46] Ruan L, Ramezani-Dakhel H, Chiu C-Y, et al. Tailoring molecular specificity toward a crystal facet: a lesson from biorecognition toward Pt{111}. *Nano Lett.* **2013**;13:840–846.
- [47] Ruan LY, Ramezani-Dakhel H, Lee C, et al. A rational biomimetic approach to structure defect generation in colloidal nanocrystals. *ACS Nano.* **2014**;8:6934–6944.
- [48] Ramezani-Dakhel H, Mirau PA, Naik RR, et al. Stability, surface features, and atom leaching of palladium nanoparticles: toward prediction of catalytic functionality. *Phys Chem Chem Phys.* **2013**;15:5488–5492.
- [49] Bedford NM, Ramezani-Dakhel H, Slocik JM, et al. Elucidation of peptide-directed palladium surface structure for biologically tunable nanocatalysts. *ACS Nano.* **2015**;9:5082–5092.
- [50] Coppage R, Slocik JM, Ramezani-Dakhel H, et al. Exploiting localized surface binding effects to enhance the catalytic reactivity of peptide-capped nanoparticles. *J Am Chem Soc.* **2013**;135:11048–11054.
- [51] Gupta A, Boekfa B, Sakurai H, et al. Structure, interaction, and dynamics of Au/Pd bimetallic nanoalloys dispersed in aqueous ethylpyrrolidone, a monomeric moiety of polyvinylpyrrolidone. *J Phys Chem C.* **2016**;120:17454–17464.
- [52] Pacardo DB, Sethi M, Jones SE, et al. Biomimetic synthesis of Pd nanocatalysts for the stille coupling reaction. *ACS Nano.* **2009**;3:1288–1296.
- [53] Tyson WR, Miller WA. Surface free energies of solid metals: estimation from liquid surface tension measurements. *Surf Sci.* **1977**;62:267–276.
- [54] Love JC, Estroff LA, Kriebel JK, et al. Self-assembled monolayers of thiolates on metals as a form of nanotechnology. *Chem Rev.* **2005**;105:1103–1170.
- [55] Heinz H. Adsorption of biomolecules and polymers on silicates, glasses, and oxides: mechanisms, predictions, and opportunities by molecular simulation. *Curr Opin Chem Eng.* **2016**;11:34–41.
- [56] Heinz H. The role of chemistry and pH of solid surfaces for specific adsorption of biomolecules in solution – accurate computational models and experiment. *J Phys: Condens Matter.* **2014**;26:244105.
- [57] Patwardhan SV, Emami FS, Berry RJ, et al. Chemistry of aqueous silica nanoparticle surfaces and the mechanism of selective peptide adsorption. *J Am Chem Soc.* **2012**;134:6244–6256.
- [58] Bolt GH. Determination of the charge density of silica sols. *J Phys Chem.* **1957**;61:1166–1169.
- [59] Emami FS, Puddu V, Berry RJ, et al. Prediction of specific biomolecule adsorption on silica surfaces as a function of pH and particle size. *Chem Mater.* **2014**;26:5725–5734.
- [60] Scott MC, Chen CC, Mecklenburg M, et al. Electron tomography at 2.4-ångström resolution. *Nature.* **2012**;483:444–447.
- [61] Chen CC, Zhu C, White ER, et al. Three-dimensional imaging of dislocations in a nanoparticle at atomic resolution. *Nature.* **2013**;496:74–77.
- [62] Miao J, Ercius P, Billinge SJL. Atomic electron tomography: 3D structures without crystals. *Science.* **2016**;353:1380.
- [63] Yang Y, Chen C-C, Scott MC, et al. Deciphering chemical order/disorder and material properties at the single-atom level. *Nature.* **2017**;542:75–79.
- [64] Ritt P, Sakidja R, Perepezko JH. Mo–Si–B based coating for oxidation protection of SiC–C composites. *Surf Coat Technol.* **2012**;206:4166–4172.
- [65] Lemberg JA, Ritchie RO. Mo-Si-B alloys for ultrahigh-temperature structural applications. *Adv Mater.* **2012**;24:3445–3480.
- [66] Rioult FA. Transient oxidation of Mo–Si–B alloys: effect of the microstructure size scale. *Acta Mater.* **2009**;57:4600–4613.
- [67] Miao JW, Förster F, Levi O. Equally sloped tomography with oversampling reconstruction. *Phys Rev B.* **2005**;72:052103.
- [68] Ma JC, Dougherty DA. The cation– π Interaction. *Chem Rev.* **1997**;97:1303–1324.
- [69] Hunter CA, Sanders JKM. The nature of π – π interactions. *J Am Chem Soc.* **1990**;112:5525–5534.
- [70] Sinnokrot MO, Sherrill CD. High-accuracy quantum mechanical studies of π – π interactions in benzene dimers. *J Phys Chem A.* **2006**;110:10656–10668.